100% internal quantum efficiency in polychiral single-walled carbon nanotube bulk heterojunction/silicon solar cells

Francesco De Nicola [a, b, *], Matteo Salvato [b, d], Carla Cirillo [e, d], Michele Crivellari [f], Maurizio Boscardin [f], Maurizio Passacantando [g], Michele Nardone [g], Fabio De Matteis [h], Nunzio Motta [c], Maurizio De Crescenzi [b], Paola Castrucci [b]

[a] *Istituto Italiano di Tecnologia, Graphene Labs, Via Morego 30, 16163 Genova, Italy*
[b] *Dipartimento di Fisica, Universita di Roma Tor Vergata, Via della Ricerca Scientifica 1, 00133 Roma, Italy*
[c] *Institute for Future Environments and School of Chemistry, Physics, and Mechanical Engineering, Queensland University of Technology (QUT), Brisbane 4001, QLD, Australia*
[d] *CNR-SPIN Salerno, Universita di Salerno, Via Giovanni Paolo II 132, 84084 Fisciano, Italy*
[e] *Dipartimento di Fisica, Universita di Salerno, Via Giovanni Paolo II 132, 84084 Fisciano, Italy*
[f] *Micro-nano Characterization and Fabrication Facility, Fondazione Bruno Kessler (FBK), Via Sommarive 18, 38123 Trento, Italy*
[g] *Dipartimento di Scienze Fisiche e Chimiche, Universita degli Studi dell'Aquila, Via Vetoio, 67100 L'Aquila, Italy*
[h] *Dipartimento di Ingegneria Industriale, Universita di Roma Tor Vergata, Via del Politecnico 1, 00133 Roma, Italy*

Abstract

Bulk heterojunction films made of polychiral single-walled carbon nanotubes (SWCNTs) form efficient heterojunction solar cells with n-type crystalline silicon (n-Si), due to their superior electronic, optical, and electrical properties. The films are multi-functional, since their hierarchical surface morphology provides a biomimetical anti-reflective, air-stable, and hydrophobic encapsulation for Si. Also, the films have a large effective area conferring them high optical absorption, which actively contribute to the solar energy harvesting together with Si. Here, we report photovoltaic devices with photoconversion efficiency up to 12% and a record 100% internal quantum efficiency (IQE). Such unprecedented IQE value is truly remarkable and indicates that every absorbed photon from the device, at some wavelengths, generates a pair of separated charge carriers, which are collected at the electrodes. The SWCNT/Si devices favor high and broadband carrier photogeneration; charge dissociation of ultra-fast hot excitons; transport of electrons through n-Si and high-mobility holes through the SWCNT percolative network. Moreover, by varying the film thickness, it is possible to tailor the physical properties of such a two-dimensional interacting system, therefore the overall device features. These results not only pave the way for low-cost, high-efficient, and broadband photovoltaics, but also are promising for the development of generic SWCNT-based optoelectronic applications.

Keywords:
Third generation solar cell Photovoltaic, Bulk heterojunction Single-walled carbon nanotube Internal quantum efficiency Silicon, Air-stable encapsulation Anti-reflective coating Hydrophobic film

* Corresponding author. Istituto Italiano di Tecnologia, Graphene Labs, Via Morego 30, 16163 Genova, Italy; *E-mail address:* francesco.denicola@iit.it (F. De Nicola).

1. Introduction

Third generation photovoltaics require a combination of low-cost and highly efficient materials in order to overcome balance of system costs. Carbon nanotubes (CNTs) are particularly attractive for their earth abundant source materials, recently scalable fabrication [1], purification methods [2], and solution processability [3]. Moreover, the unique one-dimensional properties of CNTs allow the realization of solar cells that are highly thermally conductive and mechanical, chemical, and radiation resistant [4]. In particular, single-walled carbon nanotubes (SWCNTs) have suitable photophysical properties [4] for photovoltaics, such as high aspect ratio, direct subband gaps [5], and tunable photoabsorption from the near infrared (NIR) to the ultraviolet (UV) [2]. Notably, SWCNT electronic and optical subband gaps are in a wide range: from 0.5 to 5 eV. Generally, one of the criteria for obtaining the highest photoconversion efficiency (PCE) is the correct matching of the solar cell band gap to the solar spectrum. The optimal device band gap of 1.1 eV [6] can be easily obtained from 12-15 different nanotube chirality having the first optical subband gap between 1.0 and 1.2 eV. Therefore, by using polychiral mixtures of both metallic and semiconducting SWCNTs it is possible having a broadband optical absorption in the UV-VIS-NIR range [7], harvesting in this way the majority of the solar photon flux, meanwhile avoiding the time-consuming sorting process required to isolate single-chirality distributions of SWCNTs [8]. Furthermore, the photogenerated carriers in SWCNTs are excitons with binding energies up to 0.4 eV at room temperature [9,10], which possibly may be multiple generated [11,12]. Consequently, such photogenerated excitons are ultra-fast transferred [13-15] through the SWCNT percolating network and they are dissociated into high-mobility (79000 cm^2/Vs) [16] free carriers in order to harvest their potential energy for solar cells and photodetectors. Such a dissociation is accomplished, for instance, by creating a heterojunction [17] with silicon (Si) due to the energetic band offsets greater than the SWCNT exciton binding energy [18]. In this way, charge generation, separation, transport, and collection can be realized partly by the semi-transparent, conductive SWCNT thin film and partly by Si. In addition, the large available surface area of the CNT random network films, provided by their multi-fractal hierarchical morphology [3], leads to strong and tunable optical absorption [7], anti-reflection [19] and an air-stable [20], hydrophobic encapsulation [3,21]

for Si. For all these reasons, a deep understanding of polychiral SWCNT hierarchical random networks is critical in order to realize technologically relevant photovoltaic devices. Carbon nanotube/silicon (CNT/Si) hetero- junction solar cells have steadily pushed the PCE up to 12% [22] without any post-process treatments, while up to 11% for chemically doped cells [23], 15% for integration with gold nanoparticles [8] or with anti-reflective coatings [24], and a record 17% [25] exploiting oxide layers. Despite these accomplishments, our fundamental understanding of the SWCNT/Si heterojunctions is still incomplete. Here, we report an unprecedented record 100% of internal quantum efficiency (IQE) for SWCNT/Si heterojunction solar cells. We also show for the first time that the multi-functional SWCNT film not only plays an active role in the heterojunction, but it also provides anti-reflection together with an air-stable and hydrophobic encapsulation for the solar cells. Furthermore, we introduce the SWCNT bulk heterojunction (BHJ), demonstrating that is a two-dimensional system formed by interacting SWCNTs. The optical and electrical properties of such a BHJ as well as those of the whole SWCNT/Si device are discussed. By independently optimizing the SWCNT film and Si thicknesses, we illustrate that it is possible to tailor in a controlled fashion the PCE of our solar cells up to 12±1%. Finally, we suggest a detailed model for the SWCNT/Si heterojunction.

2. Experimental

2.1. *Realization of the SWCNT films*

Highly pure single-walled carbon nanotube (SWCNT) powder (Sigma-Aldrich, CoMoCAT, assay 90%, no amorphous carbon, diameter: 0.7-1 nm) was dispersed in an aqueous solution (30 μg mL^{-1}) with 2% w/v sodium dodecyl sulfate (Sigma-Aldrich, assay > 98.5%) anionic surfactant. In order to disperse the suspension, SWCNTs were tip-ultrasonicated (Branson S250A, 200 W, 20% power, 20 KHz) in an ice-bath for an hour and the unbundled supernatant was collected by a pipette. The result was a well-dispersed suspension that was stable for several months. Single- walled carbon nanotube films were fabricated by a vacuum-filtration process of volume aliquots of the dispersion on mixed cellulose ester filters (Pall GN6, 1″ in diameter, 0.45 μm pore diameter). Subsequently, rinsing in water and in a solution of ethanol, methanol, and water (15:15:70) to remove the surfactant was performed.

2.2 Device fabrication

The substrates, provided by Fondazione Bruno Kessler (FBK), are in a top-down configuration. Au/Cr ohmic (n^+ –Si) back contact (150 nm) was evaporated on n-type crystalline Si (100) wafers ($\rho \approx 3-12$ Ω·cm, $N_D \approx 6 \cdot 10^{14}$ cm^{-3}) 4" in diameter, passivated by thermal SiO_2 (300 nm). The SiO_2 layer was patterned in two different ways by a lithographic process with a positive resist followed by a chemical etching in order to obtain a batch of devices with a 3x3 mm^2 bare Si window delimited by SiO_2. Therefore, the device active area is 0.09 cm^2. The Si wafers were made of different thickness (54-200 μm) by engraving the crystal only underneath the active area. An Au/Cr front contact electrode frame (150 nm) was then evaporated on SiO_2 by masking the Si active area. Then, wafers were cut in squares 1 x 1 cm^2. Single-walled carbon nanotube films were cut and deposited by dry-transfer printing [3,20] both on HF-etched Si active windows and on Carlo Erba soda-lime glass slides for the optical and electrical characterization.

2.2. Sample characterization

Optical spectroscopy (Agilent Cary 5000 UV/VIS/NIR) in transmission and reflection at room temperature with unpolarized light was performed on SWCNT films deposited on glass and Si. We estimated the film thickness through the Beer-Lambert law [3,7]. The SWCNT microstructure was observed by FEG-SEM (Leo 1503). The acquired micrographs were analyzed by an image software. The XPS measurements were performed on the SWCNT films deposited on Si by a PHI 1257 ESCA apparatus working in ultra-high vacuum (UHV) at a pressure of $5 \cdot 10^{-10}$ Torr. The system was equipped with a PHI 04-548 dual anode X-ray source (Al/Mg anode), a PHI 10-360 hemispherical analyzer, and a PHI 06-110 scanning electron gun. Non-monochromatic Mg X-ray source ($h\nu$=1253.6 eV) with resolution 0.8-1.0 eV was employed. Raman measurements were performed on SWCNT films deposited on Si by a LabRam high resolution Raman microscope (HORIBA Jobin Yvon) using a laser with an excitation wavelength λ = 633 nm. Electrical measurements were carried out by a Keithley 2602 A digital multimeter interfaced to a PC. Sheet resistance values were determined by van der Pauw method after measuring the electrical resistance at room temperature in standard four probe configuration. The same configuration was used to measure the electrical resistance as a function of the temperature in

a He bath, fixing the samples at the tip of a descendant in thermal contact with a Cernox thermometer. Solar cells were tested using a LOT-Oriel solar simulator under AM 1.5 G spectral illumination of 100 $mWcm^{-2}$ (1 sun). The output power density of the simulator was calibrated using a power meter. Our systematic error on the photoconversion efficiency and the fill factor is estimated by the standard deviation over five samples realized in the same way. This small uncertainty demonstrates the high reproducibility of our SWCNT/Si solar cells. External quantum efficiency was measured with a custom optical setup: a LOT-Oriel Xe lamp emits white light passing through an Applied PhotoPhysics 300-1000 nm monochromator controlled by PC. Emerging monochromatic light is focused by a lens and divided by a chopper into two beams refocused by two lenses. One beam is then detected by a Si photodiode and the other impinges on the SWCNT/Si solar cell. Both AC signals are matched by an Acquire 7265 lock-in connected to a PC. The diffuse reflectance spectra of the SWCNT/Si devices were obtained by using a combination of the Agilent Cary 5000 UV/VIS/NIR spectrometer and Agilent integrating sphere in double-beam mode at a fixed incident angle (θ=0). The total reflectance spectra were measured at a fixed incident angle ($\theta = 3^{\circ}20^{''}$), in order to collect also the specular reflectance of the samples. We characterized the wettability of SWCNT/Si solar cells, by acquiring with a custom CCD camera images of the sessile waterdrops cast on the SWCNT/Si solar cells. Static advanced contact angles were measured increasing the volume of the drop by steps of 1 μL and a plugin [26] for the open-source software ImageJ was used to estimate the contact angle values. The plugin exploits an algorithm based on a small-perturbation solution of the Young- Laplace equation. Furthermore, the presented method is applied to a continuous image of the droplet by using cubic B-Spline interpolation of the drop contour to reach the subpixel resolution. The deionized water (18.2 MΩ·cm) drop volume was V = 10 μL. Moreover, every contact angle was measured 15 s after drop castingto ensure that the droplet reached its equilibrium position.

3. Results and discussion

3.1. *Properties of the SWCNT films*

The physical properties of SWCNTs provide a new dimension for solid state physics based on the great

variety of possible geometries that are available for the nanotubes. Indeed, one of the most significant feature of SWCNTs is their one-dimensional electronic structure, which depends only on their characteristic dimension: the nanotube diameter. However, when SWCNTs are polydispersed and weaved into a macroscopic (≈cm^2) but thin (≈10-100 nm) random network film, their individual physical properties are mixed and the whole system may be considered interacting and two-dimensional, due to its high aspect ratio (10^5-10^6). We showas follow that the characteristic dimension of this two-dimensional system is not the SWCNT diameter anymore, but the film thickness indeed.

3.1.1. *Structural properties*

The SWCNT films appear as homogeneous and porous random networks of SWCNT bundles with a multi-fractal and hierarchical surface morphology [3], as shown in Fig. 1a and b. X-ray photoelectron spectroscopy (XPS) on our SWCNT films showed no trace of S or Na due to the SDS surfactant, within the experimental limit≈1% of the technique. Also Raman spectroscopy reported an amount of defects as low as 12%. Therefore, the SWCNT films realized with our method are highly crystalline, pure, and surfactant-free (see Supporting Information).

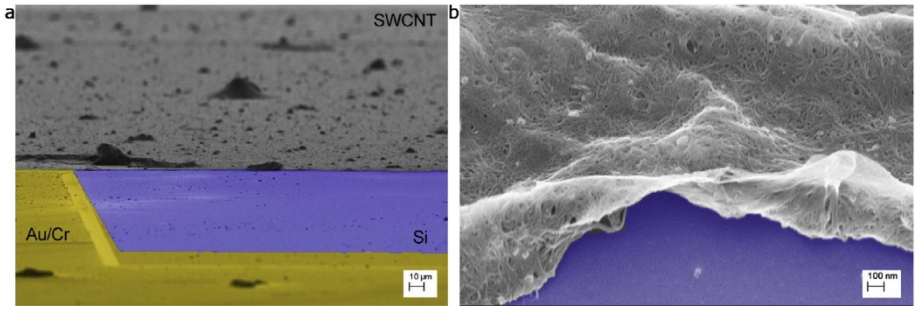

Fig. 1. Scanning electron micrographs at tilted angle (z90°) of a SWCNT film deposited on the Si substrate of a solar cell. Magnification is 1kx (a) and 100kx (b). a, The SWCNT film, which is deposited on a Si (purple false color) substrate with Au/Cr patterned electrodes (yellow false color), appears to be homogeneous and defect-free. A microstructured roughness is also shown. b, At higher magnification, it is possible to observe that the microstructured roughness is made of a nanostructured SWCNT random network, thus realizing a two-fold hierarchical surface morphology. (A colour version of this figure can be viewed online.)

3.1.2. *Optical properties*

In Fig. 2a, absorption spectra of a SWCNT film and SWCNTs in liquid dispersion are shown. The main feature of the SWCNT absorbance spectra is the π-π^* surface plasmon resonance (SPR) at 250-300 nm

[27]. Also, one-dimensional excitonic transitions are shown. By fitting the SWCNT absorbance ð Þ¼ ð Þ spectrum in Fig. 2b, we estimated 15 chirality in the range of the expected diameters 0.7-1 nm (see Supporting Information). Also, it is possible to relate the observed excitonic transitions to metallic (M_{11}, ≈10%) and semiconducting (S_{ii}, ≈ 90%) SWCNTs. Therefore, the realized films consist of polychiral semiconducting and metallic SWCNTs with diameters within 0.7-1 nm. In Fig. 2a, a broadening and a redshift of the excitonic peaks in the SWCNT film spectrum, in comparison with the spectrum of SWCNTs in liquid dispersion, can be observed. This is due to the electronic interactions among the SWCNTs [28]. It is worth noting that the peak broadening is not due to aggregation or bundling of the SWCNTs, otherwise the SPR would also broaden [29], which is not observed. The broadening of the excitonic peaks indicates the change from 1D-like to 2D-like transitions. Moreover, a 10 nm redshift toward long wavelength in the SPR, M_{11}, and S_{22} excitonic transitions can be ascribed to the change in refractive index from air (n = 1.0) to the aqueous solution with the SDS surfactant (n≈1.3) [29]. However, a 50 nm redshift occurs for S_{11} transitions. Thus, a 40 nm redshift due not to the change in refractive index but to the SWCNT interactions occurs, which in-crease the absorption edge of the overall system by ≈300 meV. Therefore, the change from a one-dimensional system to an interacting two-dimensional system can be distinguished [13,17,28]. Furthermore, the absorbance $A(\lambda)$ of our SWCNT films scales as the Beer-Lambert law $A(\lambda) = \alpha(\lambda)\tau$, where a λ is the SWCNT random network absorption coefficient [7] (see Supplementary information). Moreover, the absorption length $\delta(\lambda) = \alpha(\lambda)^{-1}$ for our SWCNT film compared with that of crystalline Si [6] is reported in Fig. 2c. Unlike Si, which has an indirect band gap of 1.12 eV, SWCNTs efficiently and uniformly absorb light from NIR to UV, bearing a wide range of direct optical subband gaps matching the solar spectrum. Typically, a 300 μm thick Si wafer is required to absorb the incident light within 1000 nm. In turn, the SWCNT random network films possess an exceptionally high absorption coefficient, which means a very low absorption length. As shown in Fig. 2c, just 24 nm thick SWCNT film is required to attenuate the incident light from the VIS to NIR range by a factor 1/e, a thickness about four orders of magnitude lower than Si. Such a high absorption is due both to the SWCNT one-dimensional electronic

properties and to their hierarchical surface morphology [19], which provide them ultra-black properties.

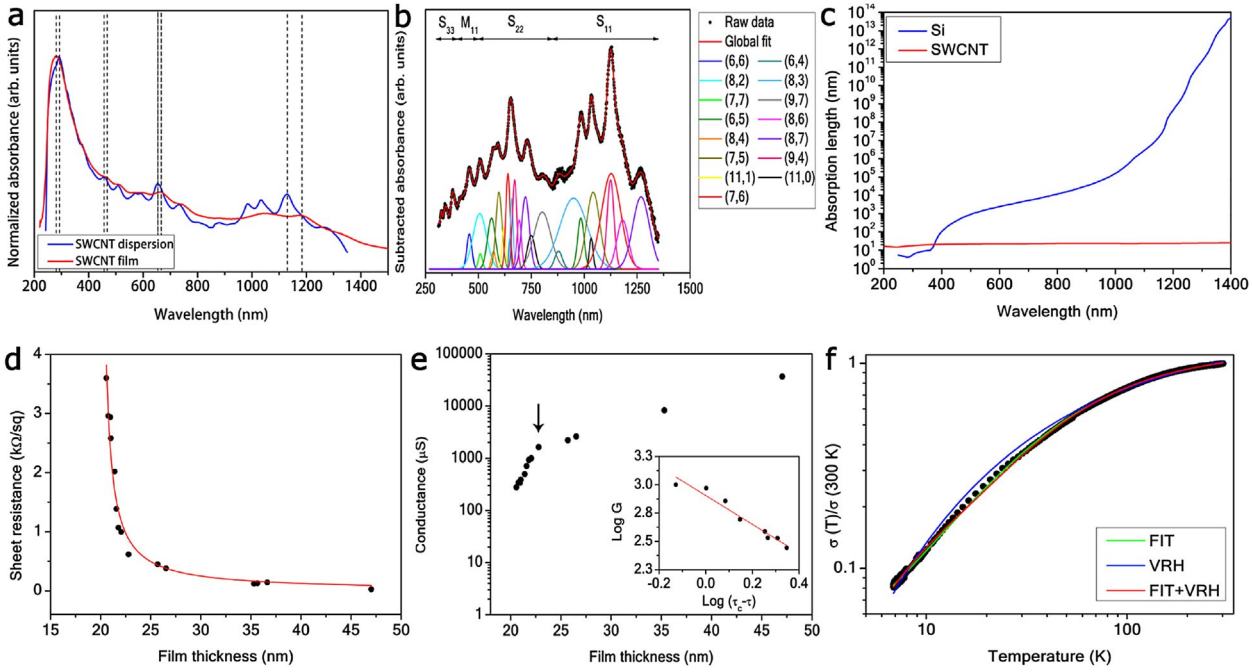

Fig. 2. a, Absorbance spectra for SWCNTs dispersed in liquid and in a film. b, Assignment of the SWCNT chirality. Four regions can be identified for our SWCNTs in liquid dispersion: 300-400 nm (S_{33}), 400-550 nm (M_{11}), 550-900 nm (S_{22}), and 800-1350 nm (S_{11}), after subtracting the SPR tail by an exponential function. The convolution function (red solid line) of the individual Voigt functions (colored solid lines) fits the SPR-subtracted absorbance spectrum (black dots) in great agreement. c, Absorption length as a function of light wavelength for Si (blue solid line) and for our SWCNT films (red solid line). d, Sheet resistance as a function of SWCNT film thickness. e, Electrical conductance of the SWCNT films in log scale as a function of the film thickness. The black arrow marks the percolation threshold $\tau_c \approx 23$ nm. The log-log plot of the conductance G as a function of the SWCNT film thickness in the inset is fitted by the conductance percolation law for $\tau < \tau_c$. f, Normalized conductivity of a 29±1 nm thick SWCNT film as function of temperature. The plot is well fitted by a linear combination of VRH and FIT models. (A colour version of this figure can be viewed online.)

3.1.3. *Electrical properties*

In Fig. 2d, the variation of the sheet resistance $R_{sh} = \rho/\tau$ with the SWCNT film thickness τ is shown. Since the sheet resistance is related to the film thickness by the SWCNT film resistivity ρ (Fig. 2d), the thicker the film, the lower the sheet resistance, as well as the transmittance values (see Supplementary information). Our SWCNT films may have low sheet resistance values with high transmittance, for instance a film 22:0±0:5 nm thick has a transmittance T (550 nm) and a sheet resistance $R_{sh} = 1$ kΩ/*sq* (see Supplementary information). From the fit in Fig. 2d, we report for our

SWCNT films $\rho=(2.5\pm0.4)\cdot10^{-6}$ Ωm, in agreement with the resistivity of multiwalled carbon nanotube (MWCNT) films [20] and bulk graphite [30]. The SWCNT film electrical conductance Gas a function of its thickness τ is reported in Fig. 2e. The plot shownin log scale follows the conductance percolation law [31] $G = G_0(\tau_c - \tau)^{\mu}$, where G_0 is the conductance of the unity of the percolation network, the thickness τ_c is the conductance percolation threshold, μ is the universal (i.e. independent of the microscopic details of the system but scale dependent) critical exponent of percolation. The percolation law is valid when $\tau < \tau_c$ and τ_c-τ is small. The plot states that as the SWCNT film thickness increases beyond the percolation threshold $\tau_c\approx23$ nm, the conductance abruptly increases following the power law as conductive paths form. Conversely, below the percolation threshold the material is non-conducting. Fitting our data in log-log scale below the percolation threshold (Fig. 2e, inset), we obtain $\mu = 1.27\pm0.11$, in agreement with the value reported for generic two-dimensional percolative systems ($\mu\approx1.33$) [31] and MWCNT films [20]. Therefore, the percolation curve shows how to optimize the two- dimensional SWCNT film making it conductive with the lowest material amount.

3.1.4. *Electronic transport properties*

When semiconducting and metallic nanostructures are blended together, the overall electronic behavior resembles that of an amorphous metal [18,32]. Indeed, the electronic transport of the individual SWCNTs in the network is not purely ballistic anymore, nor quantum [33], as it is rather dominated by disorder-induced hopping and non-resonant tunneling [18,32]. Additionally, an ultra-fast (0.2-10 ps) exciton energy transfer (EET) has been observed in SWCNT random network films [13e15]. In order to investigate the conduction mechanism for our SWCNT films, we reported in Fig. 2f the normalized conductivity $\sigma(T)=\sigma(300\ K)$ as a function of the temperature T for a SWCNT film with a thickness $\tau = 29\pm1$ nm, above the percolation threshold. The observed conductivity tends to zero as the temperature decreases, exhibiting a typical non-metallic behavior. We have been reported such a trend in conductivity also for MWCNT films [20], and generally it has been observed for disordered metals or

Fermi glasses, such as conjugated polymer films [18,32] and amorphous metals [34]. Usually, in those materials disorder and/or Coulomb interactions localize charge carriers at low temperature, inducing a metal/semiconductor transition. We fitted our data by the Mott's variable range hopping (VRH) transport [34] and the fluctuation-induced tunneling (FIT) transport [35]. However, the best fit is provided by the heterogeneous model [20,31,32], which is a linear combination of the VRH and FIT models

$$\sigma(T) = c_1\sigma_0 e^{-(T_M/T)^{\gamma}} + c_2\,\sigma_t e^{T_1/(T_0+T)} \qquad (1)$$

From the fit of the curve $\sigma(T)=\sigma(300K)$ we obtain $\sigma_0 = 0.83\pm0.02$ the temperature-independent hopping conductivity, $T_M = 178\pm3$ K the Mott's characteristic temperature, $\sigma_t = 0.33\pm0.02$ the temperature-independent tunneling conductivity, $T_1 = 10\pm1$ K the activation temperature required for an electron to tunnel through an energy barrier, $T_0 = 0.4\pm0.5$ K the minimum temperature required to activate the thermal conduction to overcome the barrier, and $\gamma = 1/(d+1) = 0.33\pm0.05$ the dimensionality dependent exponent. The fitted γ value suggests again that the system can be considered as two-dimensional ($d = 2$). Furthermore, c_1, c_2 are the normalized weights of the two transport models, which in our case state that 67% of the transport is by VRH and only 33% is by FIT. Therefore, our SWCNT films can be seen as disordered two-dimensional networks with large high-conductivity clusters separated by small low-conductivity clusters. In such a heterogeneous model, weakly localized electrons may percolate by thermally induced hopping between conducting regions, and tunnel through non-conducting regions. This description reasonably supports the fact that SWCNTs are randomly arranged with several intra- and inter-tube contacts, and local defects acting as electronic energy barriers, thus limiting the conduction [20]. Moreover, the presence of low-conductivity barrier clusters in the percolative path means that at frequencies above the semiconductor band gap the σ_{ac} will be greater than the σ_{dc}, as the former is determined by on-tube excitations and not by the inter-tube conductance [31,32]. Here, $\sigma_{ac}(550\ \text{nm})/\sigma_{dc} = 0.2$ (see Supplementary information), which means that low-conductivity barrier clusters are negligible in the SWCNT films, and the optical excitations are not fixed on SWCNTs, but are mobile from tube to tube (i.e. EET).

A BHJ [18] is a solid state blend of nanoscale materials with different electronic structures. Typically, a BHJ has a micro- structured morphology formed by spontaneous phase separation: the interfacial energy of BHJ components (donors and acceptors) favors high surface area, such that they self-assemble in order to form a microstructured and homogeneous interpenetrating network. Therefore, in a BHJ there is a donor-acceptor interface within a few nanometers, at any point of the space in the whole film volume. The optimization of such a particular morphology is required for efficient charge percolation in electronic devices. Since the exciton diffusion lengths and the carrier recombination lengths are typically on the order of tens of nanometers in nanomaterials such as SWCNTs [36], the distance between the BHJ components must be approximately within this range and defects in the inter- penetrating network must be avoided in order to not hamper the charge transport. Anyway, the morphology or the BHJ blend can be fine-tuned by controlling the solid-liquid phase separation during the film formation, by thermal annealing, or by varying the film thickness. In light of all the properties based on the experimental evidences illustrated so far for our SWCNT films, it is reasonable outlining the following considerations. Our self-assembled SWCNT films are a two-dimensional interacting system, which acts as a BHJ between the nanotubes. Despite the disordered nature of the junctions between the chirality involved in the film, a type-I heterojunction [13,17] may occur by the energy minimization principle, since charge carriers tend to propagate in regions of lower potential energy. Furthermore, when semiconducting and metallic SWCNTs are blended together the overall behavior resemble that of an amorphous metal. Also, depending on the BHJ electronic band structure, an ultra-fast EET may be achieved at the inter-tube interface throughout the SWCNT film volume, provided that the film conductivity percolation threshold has reached. Moreover, the hierarchical morphology of our SWCNT films, which mimic that of natural surfaces, provides a large accessible surface area that enables to tailor their optical properties, allowing an efficient and broadband light absorption within the thin material thickness.

3.3. *SWCNT/Si solar cells*

Sketches of the realized SWCNT/Si solar cells are shown in Fig. 3a. Despite the accomplishments in realizing SWCNT/Si solar cells, the fundamental understanding of these heterojunctions is still incomplete. Indeed, there is a strong disagreement in the scientific community on whether

SWCNT/Si devices represent Schottky, metal-insulator-semiconductor (MIS), or p-n heterojunctions [37]. However, those models cannot accurately describe the complex SWCNT/Si system. In Fig. 3b, a detailed band scheme for our SWCNT/Si heterojunction is depicted. The problem may be separated considering first the SWCNT film BHJ and then the SWCNT/Si heterojunction. As aforementioned, all the chirality assigned in our polychiral SWCNT film form a BHJ. Let us consider for simplicity only the dominant chirality (8,7), (7,6), (7,5), (6,5), (6,6), (8,2), whose absorbance is higher. Assume then that the SWCNTs are electronically intrinsic. The energy levels have been adjusted in relation to the vacuum level and equilibrated at the Fermi energy. Since the largest SWCNT diameter is ≈1 nm, each chirality has approximately the same work function Φ_{SWCNT} ~4.90 eV [38,39], but different electron affinity levels and subband gaps. In particular, in the UV-VIS-NIR range investigated five electron affinity levels $\chi^{(S)}$ can be distinguished for the considered SWCNT chirality: three for the S_1, S_2, and S_3 conduction subbands of the semiconducting SWCNTs, a $\chi^{(M)}$ for the M_1 conduction subband of the metallic SWCNTs, and a χ_{π^*} for the π^* subband, which is present in every chirality. Interestingly, although the S_1, S_2, and S_3 subbands for a given semiconducting chirality are well separated in energy by an extent higher than the thermal energy (k_BT =25 meV), the three subbands of every considered chirality are close in energy. This reflects in the formation of three well-spaced conduction and valence narrow minibands. Moreover, the M_1 subbands of metallic chirality fill the gap between the S_2 and S_3 narrow minibands. The fact that each subband is still separated from another by an energy higher than the thermal energy means that the subbands are uncoupled by a single thermal phonon and possess their own quasi-Fermi levels [6]. On the other hand, the band gap E_G and the work function Φ_{Si} of the intrinsic Si are about 1.12 eV and 4.62 eV, respectively. The conduction band position in energy of our n-Si is denoted by its electron affinity χ=4.06 eV, thus the valence band lies at 5.17 eV. In our case, for a dopant concentration of $N_D \approx 6 \cdot 10^{14}$ cm^{-3} the quasi-Fermi level is 0.32 eV below the conduction band, therefore our n-Si work function is Φ_{n-Si} =4.38 eV. When n-Si is adjoined to the SWCNT BHJ, a type-II or staggered heterojunction between the SWCNT chirality with the

smallest subband gap (0.98 eV) and Si takes place [40,41], with a built-in potential (*i.e.* the difference $\Delta\Phi$ between the Si and SWCNT work functions) $eV_{bi} = \Delta\Phi = 0.52$ eV. The maximum spatial band bending of Si for V=0 is about 4 μm. The difference in Fermi levels and electronic affinity between the SWCNT and Si leads to singularities at the junction, which favor the electron transport, while constitute a barrier for the hole transport [17]. However, these singularities are removed by the formation of the thin SiO_2 layer, which acts also as a spacer. Since the SWCNT/Si heterojunction Fermi level can be fine tuned by chemical doping, it is not pinned by SWCNT metallic subbands. Therefore, this kind of heterojunction cannot be considered just as a Schottky, nor as a p-n, or as a MIS heterojunction. It is worth noting that in SWCNT/Si solar cells the photogeneration occurs both in the Si and SWCNT films. Moreover, charge separation of photogenerated excitons in the SWCNT film occur due to the large built-in field at the interface between SWCNT films and Si. In particular, in reverse polarization ($V < 0$) hot electrons [14] photogenerated in the SWCNTs are ultra- fast transferred to the n-Si region, while hot holes are transported with high mobility [16] to the Au/Cr electrode through the SWCNT percolative network.

3.3.1. *Electrical and optoelectronic characterization*

We report in Fig. 3c the electrical response of the best SWCNT/Si (32 nm/200 μm) device in the dark state and under illumination (light state), before and after chemical doping by HNO_3 vapors for 10 s. For the undoped device, we achieved a $PCE = 8\pm1\%$, with a fill factor $FF = 42\pm7\%$. From the analysis of the light state curve (see Supplementary information), we measured the short circuit current density $J_{sc} = 34.4\pm0.1$ mA/cm^2 and the open circuit voltage $V_{oc} = 0.52\pm0.01$ V, while analyzing the dark state curve we obtained the reverse saturation current density $J_0 = (5.21\pm0.01)\ 10^{-4}$ mA/cm^2, the shunt resistance $R_p = (353\pm1)$ MΩ/cm^2, the series resistance $R_s = (144\pm2)$ Ω/cm^2, and the diode ideality factor $n = 1.32\pm0.01$.

The extremely high shunt resistance value together with the very low value of reverse saturation current density and series resistance leadto such a high value of PCE, for this kind of devices.

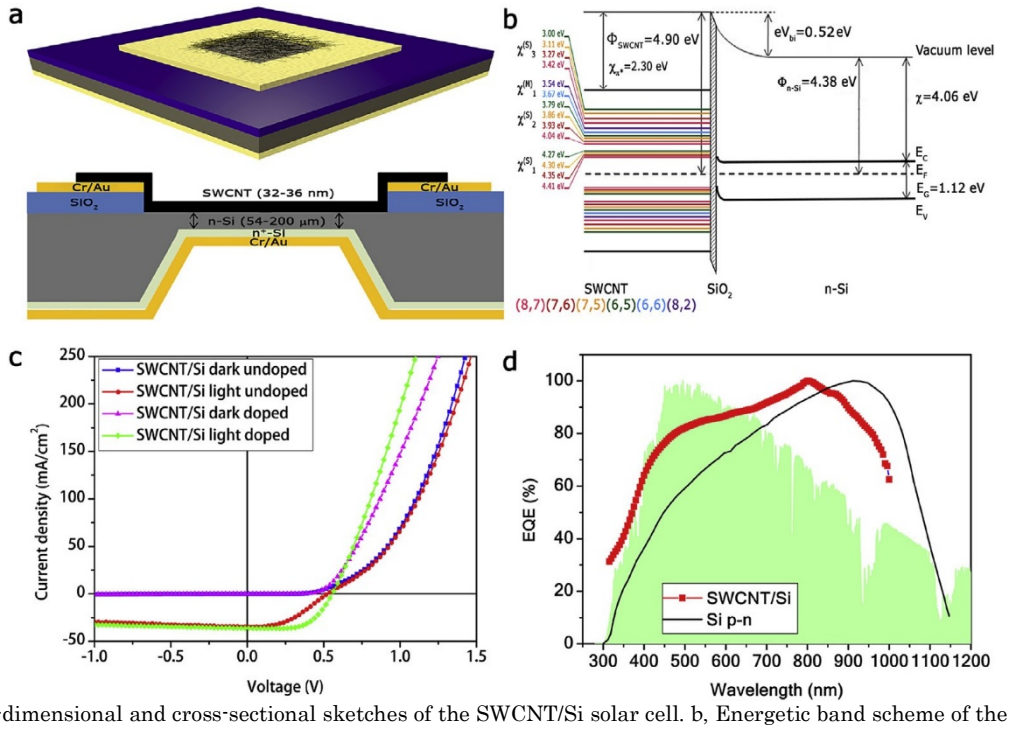

Fig. 3. a, Three-dimensional and cross-sectional sketches of the SWCNT/Si solar cell. b, Energetic band scheme of the SWCNT/Si heterojunction in reverse polarization ($V < 0$). c, Electrical response of the best SWCNT/Si device before doping under dark (blue dotted line) and under illumination (red dotted line), and after doping under dark (magenta dotted line) and under illumination (green dotted line). d, External quantum efficiency of our best device (red dotted line) in comparison with that of a reference p-n Si solar cell (black solid line) and the AM 1.5 G solar irradiance spectrum (green shaded area). Spectra are normalized to the maximum value. (A colour version of this figure can be viewed online.)

Furthermore, n is very close to the ideal value and $V_{oc} = V_{bi}$, as expected. On the other hand, for the doped device we achieved a 50% relative increment of the *FF* from 42±7% to 63±7%, therefore the *PCE* from 8±1% to 12±1%(Fig. 3c). Interestingly, after doping the dark and light state curves intersect each other, and the light state curve present a negative differential resistance in reverse polarization. These two features arerespectively hints of a higher recombination rate [42], and thedegenerate nature [43] of the SWCNT films after doping (see Supplementary information). In addition, the experimental external quantum efficiency (EQE) spectrum for our best SWCNT/Si (32 nm/200 μm) solar cell in comparison with a p-n Si reference cell (MinoltaAK200), together with the AM 1.5 G solar spectrum are reported in Fig. 3d. Spectra are normalized to the maximum value in order to highlight differences in the two devices. It is evident

from the plot that our SWCNT/Si cell has a higher efficiency in the VIS range, within one standard deviation from the solar spectrum peak. Furthermore, the SWCNT/Si heterojunction has a larger spectral interval of efficiency than the p-n Si cell, ranging from UV to VIS. Also, a large EQE contribution in the NIR above the Si band gap due tothe SWCNT absorption is expected, as it has been reported by other authors [44]. We can thus infer that the SWCNT/Si solar cells are very promising devices for third generation photovoltaics, with a high and broadband efficiency.

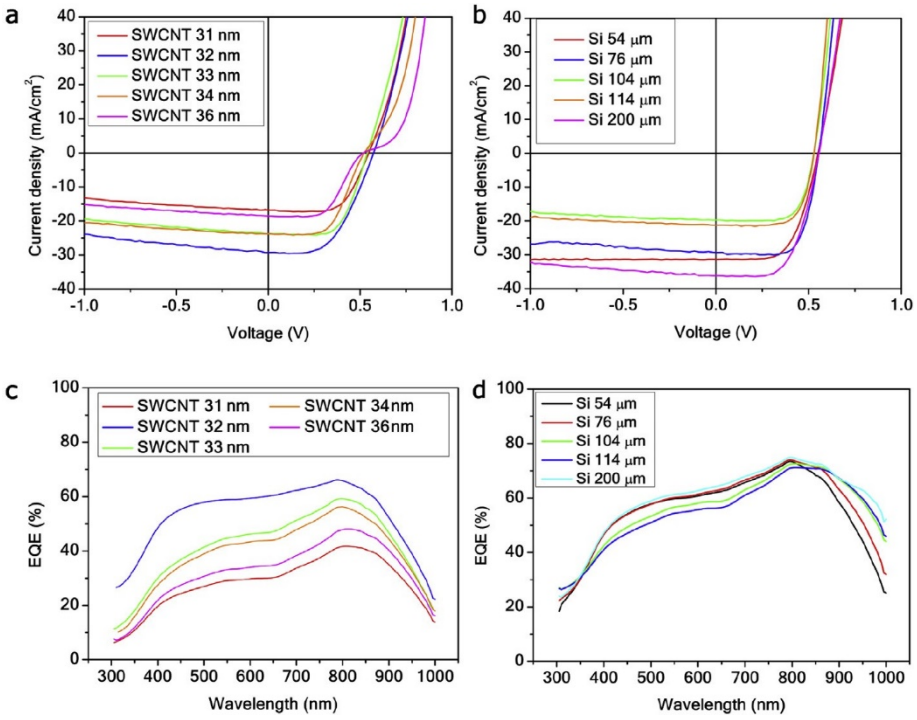

Fig. 4. Electrical response (a) and EQE (c) of the SWCNT/Si solar cell as a function of the SWCNT film thickness for a cell with 200 mm thick Si wafer. Electrical response (b) and EQE (d) of the SWCNT/Si solar cell as a function of the Si wafer film thickness for a cell with 32±5nm thick SWCNT film. (A colour version of this figure can be viewed online.)

Such an efficiency can be optimized by tailoring the SWCNT film processing and device post-treatments, as we reported for MWCNT/Si devices [20]. Here, the performance of our devices was optimized by independently fine tuning the SWCNT film and Si wafer thicknesses. We report the experimental solar cell electrical response under illumination and the EQE as a function of the SWCNT film thickness for a cell with 200 μm thick Si wafer (Fig. 4a-c), and as a function of the Si wafer thickness for a cell with 32±5 nm thick SWCNT film (in Fig. 4b-d). We can infer from data that the SWCNT/Si (32 nm/200 μm) device configuration is the best, since it has both the highest PCE and EQE. It is worth noting the large variation across the full range of the EQE as a function of the SWCNT film thickness (Fig. 4c), in comparison with the small EQE variation as a function of the Si wafer thickness (Fig. 4d). In particular, the change in the Si wafer thickness affects more the EQE at long wavelengths, where the recombination effects at the back of the device compete with the higher absorption efficiency. Indeed, these recombination effects are expected for wafers thicker than the electron diffusion length. On the other hand, the thickness change in the SWCNT films dramatically affects the whole EQE spectrum. We remark that the SWCNT exciton diffusion length has been reported to be 6-90 nm [36], consistent with our best SWCNT film thickness observed. Moreover, a film thickness of 32±5 nm is beyond the aforementioned conductance percolation threshold and absorption length, therefore the SWCNT film is well conducting and can efficiently absorb light and transport the photogenerated minority carriers through the percolative network, in order to collect them at the electrodes.

3.3.2. *Air stability*

One of the primary obstacles in realizing practical applications is the poor operational lifetime of the CNT/Si devices. Most inorganic and especially organic semiconducting materials degrade when exposed to moisture and/or oxygen. Also, photo-oxidation can be a serious problem. The degradation of devices made of such materials can be eliminated, or at least reduced to acceptable levels, by sealing the components inside an impermeable package using polymers [45-47], oxides [24], or metals [6]. Although such encapsulation methods can prevent or at least reduce oxygen and moisture permeation, they complicate the fabrication process, also resulting in increased thickness, shaded active surface, and loss

of flexibility. Typically, encapsulation is responsible for 30-40% of the material and manufacturing total costs per Wp [48]. Thus, the realization of novel methods for enhancing device lifetime is an important goal that must be accomplished without interfering with the principal device concepts. This can be achieved by enabling clean and simple device fabrication by solution processing, keeping the device flexibility and thin form factor. Since CNTs are chemically stable, the device degradation typically comes from the Si detrimental oxidation in air [49]. Recently, CNT/Si air-stable devices up to a month have been reported with [22] and without [8,20] further encapsulation. It can be observed in Fig. 5a that the PCE of our devices is fairly stable after several weeks, although they are not encapsulated. In particular, our solar cells reach a maximum of PCE after approximately three days. This fact is due to the formation of an optimal thin Si oxide layer (1-2 nm) at the CNT/Si interface [20,49]. Differently by other CNT/Si devices reported [22,23,45,47,50,51], the PCE of our solar cell does not degrade with time because of Si oxidation. Actually, the cell is stable after the oxide growth saturates (See Supplementary information).

3.3.3. *Hydrophobic properties*

We previously reported on the wetting properties of hierarchi-cal SWCNT coatings [3,21]. As shown in Fig. 5b, the solar cell Si substrate result hydrophobic after the coating by a SWCNT film, due to the petal effect, achieving a quite stable [3] contact angle value $\theta = 110 \pm 3°$, which is comparable to that of commercial hydrophobic polymers such as polydimethylsiloxane (PDMS, $\theta \approx 110^{\circ}$), currently used as encapsulating layers.

3.3.4. *Anti-reflective properties*

Anti-reflective coatings made of polymers or oxides have been employed to suppress the Si optical reflection in CNT/Si solar cells [24,45-47], hence increasing their EQE. However, those films are not broadband, being quarter-wavelength coatings, and they require a further fabrication step. We have been recently investigated the anti-reflective properties of SWCNT hierarchical random network films [19]. In particular, their hierarchical surface morphology is able to suppress the Si optical reflection over a broad range of wavelengths, angles of incidence, and for both polarizations of light, by

exploiting the moth-eye effect. Here, we show for the first time that the anti-reflective properties of these SWCNT films can be exploited for photovoltaic applications, without the need of further coatings. In Fig. 5c the total and diffuse reflectance are reported for SWCNT/Si solar cells with different SWCNT film thicknesses, and for a bare Si substrate as a control sample. It is possible to observe that the SWCNT films act as broadband anti-reflective coatings for Si. For instance, the high

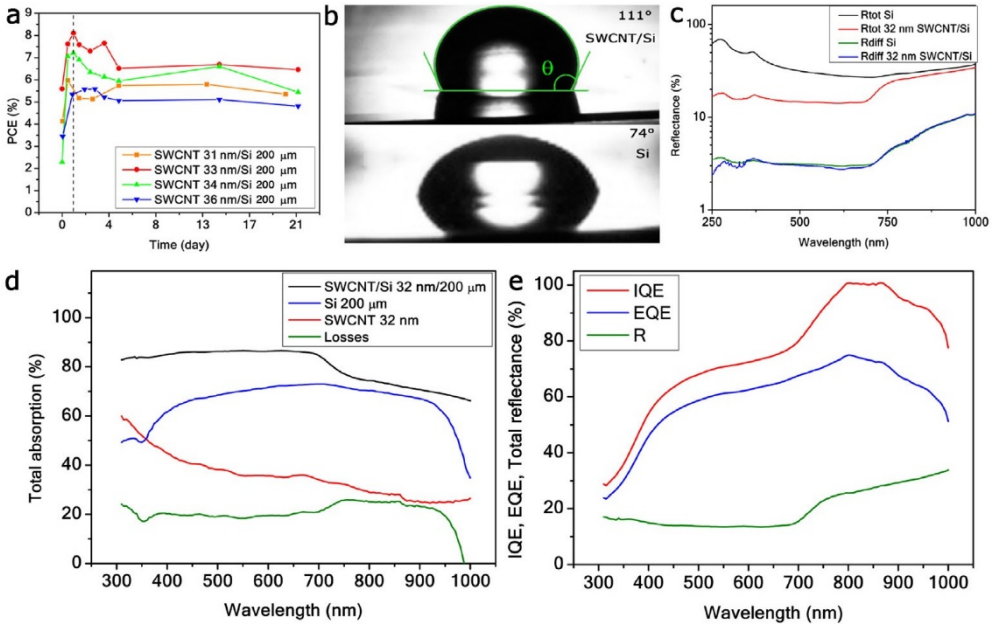

Fig. 5. a, Photoconversion efficiency of several devices with different SWCNT/Si thickness configurations as a function of the elapsed time. b, Water droplets cast on a SWCNT/Si solar cell and on a solar cell Si substrate, as a reference. c, Total (red solid line) and diffuse (blue solid line) reflectance of SWCNT/Si solar cells with 32±5 nm thick SWCNT film. As a control sample, the total (black solid line) and diffuse (green solid line) reflectance of a bare Si substrate is also reported. d Total absorption of our best SWCNT/Si (32 nm/200 μm) solar cell (black solid line), of the SWCNT film 32 nm thick (red solid line), and of the Si substrate 200 mm (blue solid line). Absorption losses (green solid line). e, Comparison among EQE, IQE, and R of our best SWCNT/Si (32 nm/200 μm) solar cell. (A colour version of this figure can be viewed online.)

total reflectance of Si (27-70%) in the UV-VIS-NIR range investigated can be reduced down to 14-33% by a SWCNT film as thin as 32±5 nm. In Fig. 5c, it is also shown that the SWCNT coatings do not vary the Si diffuse reflectance (3-10%). Although the film surface roughness is quite high (Fig. 1b), the SWCNT coatings do not behave as random scatterer surfaces, which are known to efficiently trap light inside the device [6]. Therefore, the most of the sample reflectance is specular and the anti-reflective behavior is only due to the moth-eye effect. Moreover, for the conservation of the energy $A + R + T = 1$. Since the solar cell is bulk with a reflective Au/Cr back electrode, its transmittance is $T \approx 0$. The total absorbance

$A = 1 - R$ of our best solar cell is reported in Fig. 5d, along with the total absorbance of the SWCNT film $A_{SWCNT} = 1 - R_{SWCNT} - T_{SWCNT}$, and the Si wafer $A_{Si} = 1 - R_{SWCNT\text{-}Si} - T_{SWCNT}T_{Si}$ (see Supplementary information). Thus, the light that is not reflected is partly absorbed by the SWCNT film, and partly by the Si underneath. Although the absorption coefficient of hierarchical SWCNT random networks is higher than that of Si, the Si wafer thickness is such that it absorbs the most of the incoming light. Additionally, we estimated by the quantity $(A_{Si} + A_{SWCNT} - A)/(A_{Si} + A_{SWCNT})$ a 20% of absorption losses in the solar cell. Furthermore, the internal quantum efficiency (IQE) of our best device is shown in Fig. 5e along its EQE and the total reflectance (R). We achieved a 100% record IQE in the range 795–875 nm. Such a high IQE value is truly remarkable and indicates that every absorbed photon at these wavelengths generates a pair of separated charge carriers, and they are all collected at the electrodes.

4. Conclusion

In summary, our results represent a proof-of-concept of solar cells with high efficiency and reduced cost, by integrating SWCNTs with Si. For instance, about 32 nm thick SWCNT film made of 46 μg of SWCNTs, and only 200 μm of crystalline Si are needed to make a heterojunction solar cell with PCE up to 12±1% and a EQE up to 70%. In this way, a reduction of Si about 150% with respect to conventional Si p-n solar cells has been obtained for our efficient devices. Also, the multi-functional SWCNT film form a BHJ that provides exceptional electrical and electronic properties, high and broad-band absorption, together with an anti-reflective, hydrophobic, and air-stable encapsulation. Although, our results are comparable to the best PCE values of SWCNT/Si photovoltaic cells reported by other authors (without any post-process treatments and after chemical doping), our devices further achieve a record 100% IQE at some wavelengths. Finally, the particular energy band architecture of the SWCNT films may be suitable for the realization of intermediate-band solar cells [52].

Acknowledgements

The authors acknowledge the support of the Australian Research Council through the Discovery project

DP130102120. F.D.N. gratefully acknowledges QUT for financial support. Part of the data re- ported in this paper were obtained at the Central Analytical Research Facility operated by the Institute for Future Environments(QUT). Access to CARF is supported by generous funding from the Science and Engineering Faculty (QUT). We thank the European Community for the RISE Project CoExAN GA644076. The authors declare no competing financial interests.

Appendix A. Supplementary data

Supplementary data related to this article can be found at http://dx.doi.org/10.1016/j.carbon.2016.12.050.

References

[1] K. Hata, D.N. Futaba, K. Mizuno, T. Namai, M. Yumura, S. Iijima, Water-assisted highly efficient synthesis of impurity-free single-walled carbon nanotubes, Science 306 (2004) 1362-1364.
[2] M.S. Arnold, A.A. Green, J.F. Hulvat, S.I. Stupp, M.C. Hersam, Sorting carbon nanotubes by electronic structure using density differentiation, Nat. Nanotechnol. 1 (2006) 60-65.
[3] F. De Nicola, P. Castrucci, M. Scarselli, F. Nanni, I. Cacciotti, M. De Crescenzi, Multi-fractal hierarchy of single-walled carbon nanotube hydrophobic coatings, Sci. Rep. 5 (2015) 1-9.
[4] A. Jorio, G. Dresselhaus, M.S. Dresselhaus, Carbon Nanotubes Advanced Topics in the Synthesis, Structure, Properties and Applications, Springer, New York, 2008.
[5] R. Saito, G. Dresselhaus, M.S. Dresselhaus, Physical Properties of Carbon Nanotubes, Imperial College Press, London, 1998.
[6] J. Nelson, The Physics of Solar Cells, Imperial College Press, London, 2003.
[7] F. De Nicola, C. Pintossi, F. Nanni, I. Cacciotti, M. Scarselli, G. Drera, S. Pagliara, L. Sangaletti, M. De Crescenzi, P. Castrucci, Controlling the thickness of carbon nanotube random network films by the estimation of the absorption coefficient, Carbon 95 (2015) 28-33.
[8] J.M. Harris, M.R. Semler, S. May, J.A. Fagan, E.K. Hobbie, Nature of record efficiency fluid-processed nanotube-silicon heterojunctions, J. Phys. Chem. C 119 (2015) 10295-10303.
[9] F. Wang, G. Dukovic, L.E. Brus, T.F. Heinz, The optical resonances in carbon nanotubes arise from excitons, Science 308 (2005) 838-841.
[10] F. Wang, D.J. Cho, B. Kessler, J. Deslippe, P.J. Schuck, S.G. Louie, A. Zettl, T.F. Heinz, Y.R. Shen, Observation of excitons in one-dimensional metallic single-walled carbon nanotubes, Phys. Rev. Lett. 99 (2007) 2274011-2274014.
[11] S. Wang, M. Khafizov, X. Tu, M. Zheng, T.D. Krauss, Multiple exciton generation in single-walled carbon nanotubes, Nano Lett. 10 (2010) 2381-2386.
[12] N.M. Gabor, Z. Zhong, K. Bosnick, J. Park, P.L. McEuen, Extremely efficient multiple electron-hole pair generation in carbon nanotube photodiodes, Science 325 (2009) 1367-1371.
[13] R.D. Mehlenbacher, T.J. McDonough, M. Grechko, M.-Y. Wu, M.S. Arnold, M.T. Zanni, Energy transfer pathways in semiconducting carbon nanotubes revealed using two-dimensional white-light spectroscopy, Nat. Commun. 6 (2015) 6732-6739.

[14] S. Ponzoni, G. Galimberti, L. Sangaletti, P. Castrucci, S.D. Gobbo, M. Morbidoni, M. Scarselli, S. Pagliara, Selective optical switching of interface-coupled relaxation dynamics in carbon nanotube-Si heterojunctions, J. Phys. Chem. C 118 (2014) 24110-24116.
[15] M. Grechko, Y. Ye, R.D. Mehlenbacher, T.J. McDonough, M.-Y. Wu, R.M. Jacobberger, M.S. Arnold, M.T. Zanni, Diffusion-assisted photoexcitation transfer in coupled semiconducting carbon nanotube thin films, ACS Nano 8 (2014) 5383-5394.
[16] T. Dürkop, S.A. Getty, E. Cobas, M.S. Fuhrer, Extraordinary mobility in semiconducting carbon nanotubes, Nano Lett. 4 (2004) 35-39.
[17] J.H. Davies, The Physics of Low-dimensional Semiconductors an Introduction, Cambridge University Press, Cambridge, 1998.
[18] A.J. Heeger, N.S. Sariciftci, E.B. Namdas, Semiconducting and Metallic Polymers, Oxford University Press, Oxford, 2010.
[19] F. De Nicola, P. Hines, M. De Crescenzi, N. Motta, Moth-eye effect in hierarchical carbon nanotube anti-reflective coatings, Carbon 108 (2016) 262-267.
[20] F. De Nicola, M. Salvato, C. Cirillo, M. Crivellari, M. Boscardin, M. Scarselli, F. Nanni, I. Cacciotti, M. De Crescenzi, P. Castrucci, Record efficiency of airstable multi-walled carbon nanotube/silicon solar cells, Carbon 101 (2016) 226-234.
[21] F. De Nicola, P. Castrucci, M. Scarselli, F. Nanni, I. Cacciotti, M. De Crescenzi,Exploiting the hierarchical morphology of single-walled and multi-walled carbon nanotube films for highly hydrophobic coatings, Beilstein J. Nanotechnol. 6 (2015) 353-360.
[22] F. Wang, D. Kozawa, Y. Miyauchi, K. Hiraoka, S. Mouri, Y. Ohno, K. Matsuda,Fabrication of single-walled carbon nanotube/Si heterojunction solar cells with high photovoltaic performance, ACS Photonics 1 (2014) 360-364.
[23] Y. Jia, A. Cao, X. Bai, Z. Li, L. Zhang, N. Guo, J. Wei, K. Wang, H. Zhu, D. Wu, P.M. Ajayan, Achieving high efficiency silicon-carbon nanotube heterojunction solar cells by acid doping, Nano Lett. 11 (2011) 1901-1905.
[24] E. Shi, L. Zhang, Z. Li, P. Li, Y. Shang, Y. Jia, J. Wei, K. Wang, H. Zhu, D. Wu, S. Zhang, A. Cao, TiO2-coated carbon nanotube-silicon solar cells with efficiency of 15%, Sci. Rep. 2 (2012) 1-5.
[25] F. Wang, D. Kozawa, Y. Miyauchi, K. Hiraoka, S. Mouri, Y. Ohno, K. Matsuda, Considerably improved photovoltaic performance of carbon nanotube-based solar cells using metal oxide layers, Nat. Commun. 6 (2015) 6305-6312.
[26] A.F. Stalder, T. Melchior, M. Müller, D. Sage, T. Blu, M. Unser, Low-bond axisymmetric drop shape analysis for surface tension and contact angle measurements of sessile drops, Colloid Surf. A 364 (2010) 72-81.
[27] Y. Murakami, E. Einarsson, T. Edamura, S. Maruyama, Polarization dependence of the optical absorption of single-walled carbon nanotubes, Phys. Rev. Lett. 94 (2005) 0874021-0874024.
[28] H.T. Grahn, Semiconductor Superlattices: Growth and Electronic Properties, World Scientific, Singapore, 1995.
[29] C.S.S.R. Kumar, UV-VIS and Photoluminescence Spectroscopy for Nanomaterials Characterization, Springer, New York, 2013.
[30] P. R. Wallace, The band theory of graphite, Phys. Rev. 71.
[31] M. Sahimi, Applications of Percolation Theory, CRC Press, Boca Raton, 2009.
[32] A.B. Kaiser, Electronic transport properties of conducting polymers and carbon nanotubes, Rep. Prog. Phys. 64 (2001) 1-49.
[33] C. Dekker, Carbon nanotubes as molecular quantum wires, Phys. Today 52 (1999) 22-28.
[34] N.F. Mott, Electrons in disordered structures, Adv. Phys. 16 (1967) 49-144.
[35] P. Sheng, Fluctuation-induced tunneling conduction in disordered materials, Phys. Rev. B 21 (1980) 2180-2195.
[36] L. Lüer, S. Hoseinkhani, D. Polli, J. Crochet, T. Hertel, Size and mobility of excitons in (6, 5) carbon nanotubes, Nat. Phys. 5 (2009) 54-58.
[37] D.D. Tune, B.S. Flavel, R. Krupke, J.G. Shapter, Carbon nanotube-silicon solar cells, Adv. Energy Mater. 2 (2012) 1043-1055.
[38] W.S. Su, T.C. Leung, C.T. Chan, Work function of single-walled and multiwalled carbon nanotubes: first-principles study, Phys. Rev. B 76 (2007)
2354131-2354138.
[39] M. Shiraishi, M. Ata, Work function of carbon nanotubes, Carbon 39 (2001) 1913-1917.
[40] M. Gong, T.A. Shastry, Y. Xie, M. Bernardi, D. Jasion, K.A. Luck, T.J. Marks, J.C. Grossman, S. Ren, M.C. Hersam, Polychiral semiconducting carbon nanotube-fullerene solar cells, Nano Lett. 14 (2014) 5308-5314.

[41] B.J. Landi, S.L. Castro, H.J. Ruf, C.M. Evans, S.G. Bailey, R.P. Raffaelle, Cdse quantum dot-single wall carbon nanotube complexes for polymeric solar cells, Sol. Energy Mater. Sol. Cells 87 (2005) 733-746.
[42] J. Nelson, J. Kirkpatrick, P. Ravirajan, Factors limiting the efficiency of molecular photovoltaic devices, Phys. Rev. B 69 (2004) 0353371-03533711.
[43] S.M. Sze, Physics of Semiconductor Devices, John Wiley & Sons, New York, 1969.
[44] J. Lehman, A. Sanders, L. Hanssen, B. Wilthan, J. Zeng, C. Jensen, Very black infrared detector from vertically aligned carbon nanotubes and electric-field poling of lithium tantalate, Nano Lett. 10 (2010) 3261-3266.
[45] Y. Jia, P. Li, X. Gui, J. Wei, K. Wang, H. Zhu, D. Wu, L. Zhang, A. Cao, Y. Xu, Encapsulated carbon nanotube-oxide-silicon solar cells with stable 10% efficiency, Appl. Phys. Lett. 98 (2011) 1331151-1331154.
[46] R. Li, Iangtao Di, Z. Yong, B. Sun, Q. Li, Polymethylmethacrylate coating on aligned carbon nanotubesilicon solar cells for performance improvement, J. Mater. Chem. A 2 (2014) 4140-4143.
[47] L. Yu, D.D. Tune, C.J. Shearer, J.G. Shapter, Implementation of antireflection layers for improved efficiency of carbon nanotubesilicon heterojunction solar cells, Sol. Energy 118 (2005) 592-599.
[48] S.A. Mann, M.J. de Wild-Scholten, V.M. Fthenakis, W.G.J.H.M. van Sark, W.C. Sinke, The energy payback time of advanced crystalline silicon PV modules in 2020: a prospective study, Prog. Photovolt. Res. Appl. 22 (2014) 1180-1194.
[49] C. Pintossi, S. Pagliara, G. Drera, F. De Nicola, P. Castrucci, M. De Crescenzi, M. Crivellari, M. Boscardin, L. Sangaletti, Steering the efficiency of carbon nanotube-silicon photovoltaic cells by acid vapor exposure: a real-time spectroscopic tracking, ACS Appl. Mater. Interfaces 7 (2015) 9436-9444.
[50] Y. Jia, A. Cao, F. Kang, P. Li, X. Gui, L. Zhang, E. Shi, J. Wei, K. Wang, H. Zhu, D. Wu, Strong and reversible modulation of carbon nanotube-silicon heterojunction solar cells by an interfacial oxide layer, Phys. Chem. Phys. 14 (2012) 8391-8396.
[51] K. Cui, A.S. Anisimov, T. Chiba, S. Fujii, H. Kataura, A.G. Nasibulin, S. Chiashi, E.I. Kauppinen, S. Maruyama, Air-stable high-efficiency solar cells with drytransferred single-walled carbon nanotube films, J. Mater. Chem. A 2 (2014) 11311-11318.
[52] A. Luque, A. Martí, C. Stanley, Understanding intermediate-band solar cells, Nat. Photon. 6 (2012) 146-152.